

Article

Fabrication of Piezoelectric ZnO Nanowires on Laser Textured Copper Substrate to Enhance Catalytic Properties

Hongbin Wang¹, Rui Zhou^{1,2,*} , Huangping Yan¹  and Hongjun Liu^{3,4,*}

¹ Pen-Tung Sah Institute of Micro-Nano Science and Technology, Xiamen University, Xiamen 361005, China; 19920211151488@stu.xmu.edu.cn (H.W.); hpyan@xmu.edu.cn (H.Y.)

² Innovation Laboratory for Sciences and Technologies of Energy Materials of Fujian Province (IKKEM), Xiamen 361005, China

³ Key Laboratory of Natural Medicine and Immuno-Engineering of Henan Province, Henan University, Kaifeng 475004, China

⁴ Water Technology Research Center, AGplus Technologies Co., Ltd., Huizhou 516082, China

* Correspondence: rzhou2@xmu.edu.cn (R.Z.); hjliu@henu.edu.cn (H.L.)

Abstract: In this work, 3D periodic “grid-type” CuO/Cu₂O layers were fabricated on a copper sheet using laser processing techniques, and the laser processing parameters were optimized for favorable ZnO nanowire growth. It was found that ZnO nanowires could be successfully prepared to form a CuO-Cu₂O-ZnO heterojunction structure without an extra catalyst or seed layer coating, which could be attributed to the copper oxide active sites induced via laser texturing. ZnO nanowires on laser textured “grid-type” copper substrates demonstrated an effective piezocatalytic performance with different morphologies and the generation of abundant reactive oxygen species in the CuO-Cu₂O-ZnO catalytic system, providing a fundamental mechanism for the degradation of organic dye in water. This simple and low-cost method could provide a useful guide for the large-scale efficient and versatile synthesis of immobilized piezoelectric catalysts.

Keywords: laser processing; ZnO heterojunction; piezocatalytic; wastewater treatment



Citation: Wang, H.; Zhou, R.; Yan, H.; Liu, H. Fabrication of Piezoelectric ZnO Nanowires on Laser Textured Copper Substrate to Enhance Catalytic Properties. *Coatings* **2023**, *13*, 1963. <https://doi.org/10.3390/coatings13111963>

Academic Editor: Rosalba Passalacqua

Received: 28 September 2023
Revised: 9 November 2023
Accepted: 10 November 2023
Published: 17 November 2023



Copyright: © 2023 by the authors. Licensee MDPI, Basel, Switzerland. This article is an open access article distributed under the terms and conditions of the Creative Commons Attribution (CC BY) license (<https://creativecommons.org/licenses/by/4.0/>).

1. Introduction

Over the past few decades, as the adverse effects of rapid global industrialization have intensified, water pollution has become a serious global problem that poses a major challenge to the sustainable development of human civilization. Therefore, research into the removal of contaminants from natural water systems is urgent and necessary. Among various water treatment solutions, utilizing energy from nature to purify water sources is likely to be the most promising technology because it is a green, energy-saving, and facile method [1–3]. Currently, piezoelectric catalysts such as BaTiO₃ [4], MoS₂ [5,6], TiO₂ [7], and ZnO [8] have been widely studied and reported. Among them, ZnO nanowires have shown excellent performance in harvesting mechanical energy in the natural environment (such as wind energy, tidal energy, energy from acoustic waves, and atmospheric pressure) [9–12], and can be applied in the fabrication of piezoelectric nanogenerators [13–15], high-performance visible/ultraviolet photoelectric detectors [16,17], the decomposition of water to produce sustainable hydrogen fuel [18,19], and wastewater treatment in industry, etc. When ZnO nanowires are deformed under the action of an external force, a piezoelectric field can be generated on the surface, which induces electrons and holes in the nanowires to migrate in opposite directions [20], and the separated charges react with oxygen and OH[−] in the water and produce reactive oxygen species (ROS) that continuously degrade pollutants in the water [21]. However, the high recombination rate of separated electron–hole pairs during piezoelectric catalytic degradation consumes external input mechanical energy and reduces piezoelectric catalytic efficiency. Many efforts

have been made to prevent the recombination of electron–hole pairs, such as the development of various novel ZnO nanostructures [22–24], the construction of efficient ZnO nanowire heterojunctions [25–27], the introduction of external electric fields, and the coupling of piezoelectric with photoelectric effects of ZnO nanowires [28,29]. Among them, the construction of heterojunctions is considered to be one of the most effective methods to improve the efficiency of electron and hole separation within ZnO nanowires, such as ZnO-CuO [30], ZnO-CeO₂ [31], ZnO-Au@Pt [32], ZnO-GO [33], ZnO-Ag [34], etc. These as-prepared hybrid catalysts are mainly divided into non-immobilized and immobilized catalysts, which have inherent limitations in their use. For example, non-immobilized catalysts are prone to the introduction of secondary contamination in operation and cannot be used on a large scale. Most immobilized catalysts require a seed layer to be implemented before the reaction, and their high cost and complex fabrication processes likewise limit their practical application at the industrial level [35]. Therefore, it is of great significance to develop a seed-layer-free, immobilized ZnO catalyst fabrication process.

Recently, some works have reported the seedless hydrothermal synthesis of ZnO-immobilized catalysts. However, most of them required expensive single-crystal substrates (e.g., GaN [36]), deposited Ti/Au film [37], or the introduction of an external electrical field to enhance the ZnO nucleation [38]. Therefore, the preparation of periodic and patterned arrays of CuO-Cu₂O-ZnO heterojunction on 3D micro-/nano-structured copper substrates remains a great challenge. In recent years, laser processing technology has attracted a lot of attention in the preparation of water treatment materials due to its unique advantages such as high energy density and short processing time [39–41], including processing various superhydrophobic surfaces with self-cleaning functions and preparing graphene materials with anti-fouling and anti-bacterial functions [42,43]. Our group also reported the fabrication of copper mesh with an oil–water separation function using laser processing technology for oil spill treatment in the environment, along with other uses [44,45]. The unique advantages of laser processing technology have opened up a new path for the development of efficient water treatment materials.

In this work, a laser-processing-technique-assisted hydrothermal method was proposed to fabricate a CuO-Cu₂O-ZnO heterojunction array with efficient piezoelectric catalytic capacity for water purification, where a periodic three-dimensional CuO-Cu₂O-Cu substrate was fabricated via laser ablation, followed by the hydrothermal-synthesis-induced growth of ZnO nanowires on a 3D CuO-Cu₂O-Cu substrate for the formation of a CuO-Cu₂O-ZnO heterojunction structure. The CuO-Cu₂O-Cu substrates generated via laser processing simplified the hydrothermal growth process of ZnO nanowires and helped to promote the separation of electron and hole pairs inside ZnO nanowires, improving their piezoelectric catalytic water purification capability. The piezocatalytic activity of the CuO-Cu₂O-ZnO heterojunction array was evaluated via MB decomposition under ultrasonic vibration in the dark. The results showed that the CuO-Cu₂O-ZnO heterojunction array possessed up to 34% degradation capacity within 30 min. Furthermore, the hydroxyl radicals and superoxide anions generated during piezoelectric catalysis were detected via the terephthalic acid photoluminescence (TA-PL) method and the nitroblue tetrazolium (NBT) transformation method, respectively. The results showed that a large amount of reactive oxygen species were generated in the CuO-Cu₂O-ZnO catalytic system, which provided a basic mechanism for the degradation of organic dyes in water. The combination of the unique advantages of laser processing technology and hydrothermal methods could provide a highly efficient and cost-effective method for developing new and versatile immobilization catalysts.

2. Materials and Methods

2.1. Materials

All of the chemicals were of analytical grade and used without further purification. Zinc nitrate hexahydrate (Zn(NO₃)₂·6H₂O, 1 mol/L), copper sheet, hexamethylenete-

tramine (HMTA; $C_6H_{12}N_4$, 30 wt%), ammonia water, terephthalic acid (TA), and nitroblue tetrazolium (NBT) were obtained from Aladdin Chemistry Co. Ltd. (Shanghai, China).

2.2. Preparation of Periodic 3D CuO-Cu₂O-ZnO Heterojunction Array

The copper sheet, with a thickness of $\approx 300 \mu\text{m}$, was cut into pieces of around $1 \text{ cm} \times 1 \text{ cm}$ and cleaned with deionized water, followed by hotplate drying. A nanosecond pulsed laser ablation system was applied to create a patterned “grid-type” substrate microstructure in ambient air, as shown in Figure 1a. A laser with a wavelength of 1064 nm, pulse repetition rate (PRR) of 25 kHz, spot size of $\approx 30 \mu\text{m}$, scanning speed of 500 mm s^{-1} , and scan line spacing of $\approx 0.05 \text{ mm}$ was used, whereas the number of scanning repetitions was set at 1, 5, and 10, respectively. To optimize laser processing parameters for the growth of ZnO nanowires, $Zn(NO_3)_2$ and HMTA reactant concentrations at 50 mM in 3 M ammonia aqueous solution were chosen to prepare the ZnO nanowire growth solution, and then the solution was transferred to a 25 mL reaction kettle and stirred with a glass rod for one minute to mix it well. Then, we placed the processing surface of the copper sheet downward against the inner wall of the reaction kettle. The reaction temperature was set to $150 \text{ }^\circ\text{C}$ and the growth time was two hours. After the reaction, the copper sheets were removed, rinsed several times with deionized water, and placed on a drying table at $100 \text{ }^\circ\text{C}$ to dry. Figure 1b,c shows a schematic diagram of hydrothermally grown ZnO nanorods on the “grid-type” substrate. The laser processing parameters for the “grid-type” substrate were set at 10 rounds of laser scanning and spot line spacing of $50 \mu\text{m}$. ZnO nanowires were obtained under hydrothermal conditions in 3 M ammonia aqueous solution with both $Zn(NO_3)_2$ and HMTA reactant concentrations of 1 mM, 25 mM, 50 mM, 100 mM, 200 mM, 400 mM, 600 mM, and 800 mM (molar concentrations and volume ratios, $Zn(NO_3)_2$:HMTA = 1:1), respectively, which are labeled as S1, S2, S3, S4, S5, S6, S7, and S8, in order.

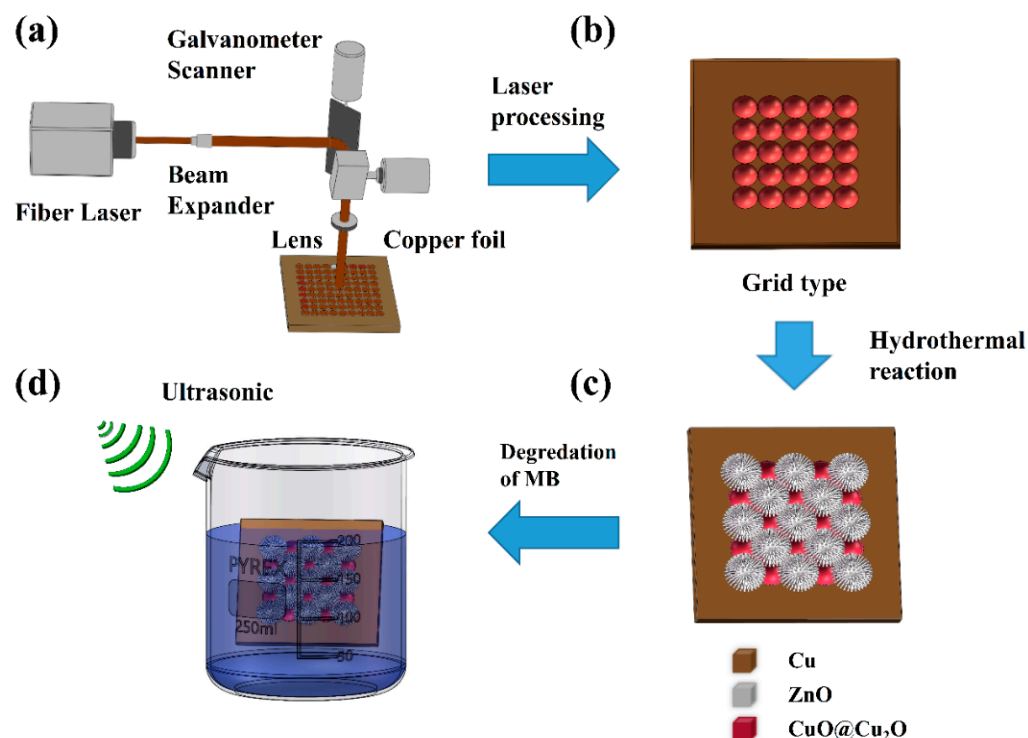


Figure 1. (a) Schematic diagram of the principle of laser processing of “grid-type” substrate. (b,c) Hydrothermal growth of ZnO nanorods on copper sheet. (d) Schematic diagram of the degradation of MB solution via ultrasonication.

2.3. Mechanical Stability of ZnO Nanowires on Laser Ablated Substrate

The adhesion of the ZnO nanowires was tested using an ultrasonic cleaning experiment. First, the grid-type substrate was put in a beaker. A total of 20 mL of deionized water was added, and it was treated in an ultrasonic cleaner with 120 W power for 5 min; then, it was placed on a drying table at 100 °C to dry it.

2.4. Piezocatalytic Performance Evaluation

As shown in Figure 1d, in order to test the catalytic activity of the CuO-Cu₂O-ZnO catalysts, 0.3 mg of methylene blue powder was dissolved in 500 mL of deionized water, and then 30 mL of methylene blue solution was taken out at a time to conduct the catalytic degradation experiment, ensuring the same initial concentration of MB at the beginning of each experiment for each experimental group. At room temperature, each group of samples was placed into beakers containing MB solution and kept in the dark for 5 min to reach dissociation and adsorption equilibrium. The beaker was then placed in an ultrasonic cleaner with 120W and a frequency of 40 kHz for degradation experiments. After taking out 3–4 mL of the solution every five minutes and performing centrifuge treatment, the change in MB concentration was measured using a UV-Vis spectrophotometer. To prevent the effect of heat generated from ultrasonic vibrations, the water in the ultrasonic cleaner was changed every ten minutes until the experiment was completed. The catalytic capacity was defined as $C/C_0 \times 100\%$; the corresponding degradation rate was defined as $(1 - C/C_0) \times 100\%$; C_0 was the concentration of MB at $T = 0$ min when the adsorption equilibrium was reached; and C was the concentration of MB after 30 min of catalysis [46].

2.5. Active Species Trapping

Radical trapping experiments were carried out to identify the primary reactive oxygen species (ROS) generated in each of the eight CuO-Cu₂O-ZnO heterojunction array systems. To identify the ·OH radicals, the reaction of terephthalic acid (TA) with ·OH to produce the highly fluorescent 2-hydroxy terephthalic acid (TAOH) was investigated. At fixed time intervals of the piezocatalytic treatment, an aliquot of the solution was withdrawn and transferred in a cuvette, and the PL spectrum was recorded using a fluorescence spectrometer operating at an excitation wavelength of 315 nm and an emission wavelength of 429 nm. To detect the radical ·O₂⁻ formed under piezocatalytic conditions, a reaction was carried out of NBT with ·O₂⁻ to form the insoluble purple formazan, spectrophotometrically monitoring the changes in the concentration of NBT. For this purpose, an NBT solution with a concentration of 0.03 mM was prepared and the UV-Vis spectra of the solution were recorded at different times of reaction; we observed a continuous decrease in the NBT absorption maximum centered at 259 nm as the reaction proceeded and the reagents were consumed.

Firstly, a 5 mM terephthalic acid solution was prepared in a NaOH solution (10 mM) to analyze the radical of ·OH. Then, 20 pieces of experimental samples were added to 45 mL of the above solution and exposed to ultrasonic irradiation. The fluorescence spectra were recorded using a fluorescence spectrometer operating at an excitation wavelength of 315 nm and an emission wavelength of 429 nm. NBT reacted with ·O₂⁻ to form the insoluble purple formazan, thus leading to a decrease in absorbance at 259 nm. The NBT solution was prepared with a concentration of 0.03 mM. The production of ·O₂⁻ could be tested by monitoring the concentration change in NBT using a UV-Vis spectrophotometer (PerkinElmer, USA).

2.6. Characterization

The surface morphology, composition, and chemical valence of the samples were studied via scanning electron microscopy (SEM, Germany, GeminiSEM 500), X-ray powder diffraction (Japan, Shimadzu XRD-7000), and X-ray photoelectron spectroscopy (XPS, USA, Thermo Scientific, ESCALAB Xi+). The efficiency of MB degradation using CuO-Cu₂O-ZnO catalysts and the detection of superoxide anion production during piezoelectric catalysis

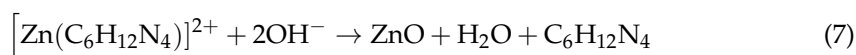
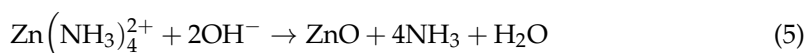
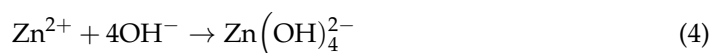
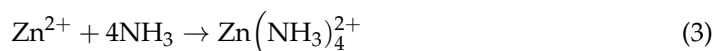
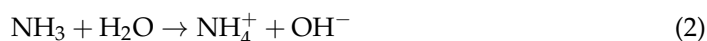
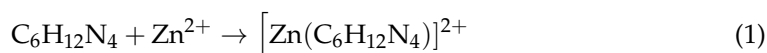
were examined via UV-Vis spectroscopy (USA, LAMBDA 1050+). The hydroxyl radical production was detected via transient fluorescence spectroscopy (UK, Edinburgh FLS1000, FLS1000).

3. Results and Discussion

3.1. Growth of ZnO Nanowires on Laser Textured Copper Substrate

Figure 2a,b shows the “grid-type” substrate fabricated on a copper sheet using laser processing techniques. The regular 3D “dimple” pits were left where the laser spot scanned [47], “tapered bumps” were formed in the middle of every four 3D “dimple” pits, and a large number of nanoparticles and inhomogeneous corrugated transition layers were deposited next to them. The regular 3D “dimple” pits and 3D “tapered bumps” were vertically cross-distributed with a diameter of about 40 μm on the bottom. These experimental results can be explained in terms of a dynamic ablation process using a laser. At high laser fluences, the ablated copper atoms are anisotropically ejected into the air with a plasma plume formation, demonstrating the high kinetic energy of the species. Then, the plasma strongly interacts with the air molecules, leading to plasma nucleation and oxidation of the copper atoms, forming nanoparticles and aggregate. Finally, these particles are deposited on the copper surface under the operation of gravity and air resistance [48].

From Figure 2c, it can be seen that large amounts of CuO and Cu₂O were produced on the surface of the 3D “grid-type” substrate, which are key to growing ZnO without a catalyst or seed layer coating. The physical reason for such enhanced nucleation and regular growth in the presence of CuO-Cu₂O heterojunction may be attributed to a galvanic effect in the substrate [49]. Although the system is quite complex, we have represented the main chemical reactions in the following equations [50]:



Under the action of the built-in electric field of the CuO-Cu₂O heterojunction, the positively charged intermediates $\text{Zn}(\text{NH}_3)_4^{2+}$, $[\text{Zn}(\text{C}_6\text{H}_{12}\text{N}_4)]^{2+}$, and OH^- formed in the hydrothermal reaction migrate towards the substrate containing CuO and Cu₂O and then react to form ZnO crystals. These enable the laser-processed copper substrate to grow ZnO nanorods without any catalyst or seed layer coating, which is consistent with recent investigations into the Al-based galvanic-cell effect for synthesizing ZnO nanorods on conducting substrates [51].

Figure 2d–i shows the SEM images of the ZnO nanowires, grown via hydrothermal synthesis, on “grid-type” substrates prepared using different numbers of laser scans. The patterned ZnO nanowire arrays mainly consisted of nanorods with pinpoint tops, which were densely and uniformly distributed on the “grid-type” substrate. The nanorod lengths were in the range of 1–5 μm . Furthermore, as the number of laser scans increased, more and more ZnO nanowires were grown on the substrate, which were attributed to the

greater number of induced copper oxide active sites as the number of laser scans increased. The XRD patterns of the 3D “grid-type” substrates prepared with different numbers of laser scans are shown in Figure 2c. As the number of laser scans increased, the peak intensity of copper decreased, relative to that of CuO and Cu₂O, indicating that the copper substrate was more severely ablated by the laser, resulting in a larger surface area of the copper substrate being oxidized, producing more CuO-Cu₂O particles and inhomogeneous corrugated transition layers, which is beneficial for the growth of ZnO nanowires.

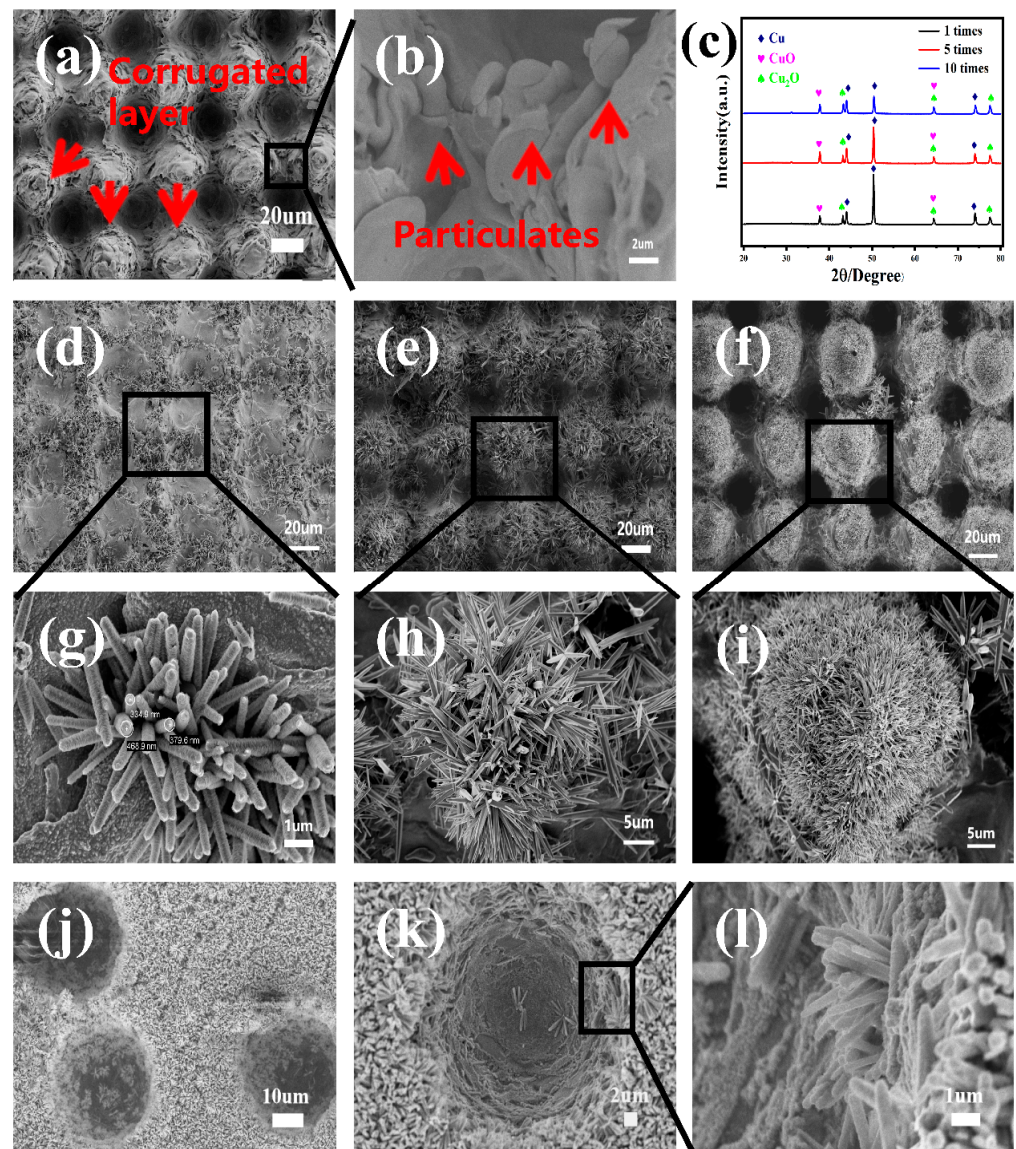


Figure 2. (a,b) “Grid-type” substrates and 10 rounds of laser spot scanning; (c) XRD patterns of the substrate after a number of laser scanning repetitions of 1, 5, and 10; (d–i) hydrothermal growth of ZnO nanowires on “grid-type” substrates with different laser processing parameters; (d,g) 1 round of laser spot scanning; (e,h) 5 rounds of laser spot scanning; (f,i) 10 rounds of laser spot scanning; (j–l) adhesion test for ZnO nanowires; (j) before ultrasonic cleaning for 5 min; (k,l) after ultrasonic cleaning for 5 min.

The long-term performance of immobilized hybrid catalysts is governed by the stability and adhesion of ZnO nanowires to the immobilizing substrate. Ultrasonic cleaning experiments for ZnO nanowires are shown in Figure 2j–l. Figure 2j shows the SEM images before ultrasonic stripping, and Figure 2k,l shows the SEM images after ultrasonic cleaning in deionized water for 5 min. The figure shows that most of the ZnO nanowires remain on

the copper sheet, which further indicates the strong adhesion of the ZnO nanowires grown on the copper sheet [52]. As shown in Figure 2a,b, a large number of nanoparticles, regular pits [53], and corrugated transition layers were produced on the copper sheet, increasing the roughness of the substrate surface, which may be one of the important reasons for the strong adhesion of ZnO nanowires on the 3D CuO-Cu₂O substrate [54,55].

Figure 3a shows the XRD pattern of the CuO-Cu₂O-ZnO heterojunction constructed on a copper sheet. The sharp diffraction peaks indicate that the grown ZnO nanowires exhibit a good crystalline quality, and all of the diffraction peaks correspond to the wurtzite structured ZnO (JCPDS card no. 36-1451) [56]. Other peaks are attributed to the Cu (JCPDS card no. 04-0836), Cu₂O (JCPDS card no.99-0041), and cubic CuO (JCPDS card no. 71-0251) [57]. This demonstrates the successful preparation of CuO-Cu₂O-ZnO heterojunction catalysts on a “grid-type” substrate. We further analyzed the elemental valence state of the substrate copper surface after laser processing via XPS. Figure 3b shows the XPS scan spectrum of a “grid-type” copper sheet after the hydrothermal growth of ZnO nanowires, and from which the main binding energy peaks of carbon (C 1s), oxygen (O 1s), zinc (Zn 2p), and copper (Cu 2p) can be observed. As shown in Figure 3c, the peak at binding energy of 935.2 eV corresponds to CuO [58], while the peak at binding energy of 933.5 eV corresponds to Cu₂O [59]. This is a good indication of the generation of CuO and Cu₂O on the copper surface after laser processing. The XPS spectrum of Zn 2p is shown in Figure 3d and the two strong peaks at binding energies of 1023.06 eV and 1046.20 eV correspond to Zn 2p^{3/2} and Zn 2p^{1/2}, respectively, which indicates the presence of Zn in the form of ZnO. Figure 3e shows the XPS spectra of C 1S, and the three strong peaks at binding energies 284.8 eV, 286.5 eV, and 288.7 eV can be assigned to the C-C bond, C-O-C bond, and HO-C=O bond, respectively. Figure 3f shows the spectra of O 1S, and the three strong peaks at binding energies 530.1 eV, 531.5 eV, and 532.5 eV can be seen to originate from the Cu-O bond, Zn-OH bond, and -OH bond. It has been documented that these oxygen-containing functional groups facilitate the anchoring of ZnO nanorods [33].

In this section, 3D periodic “grid-type” CuO-Cu₂O-ZnO heterojunctions were successfully fabricated via the laser-processing-technique-assisted hydrothermal method, and the laser processing parameters were optimized for favorable ZnO nanowire growth. The CuO-Cu₂O-ZnO heterojunction structure was further verified by XRD and XPS characterizations. Furthermore, it was found that laser-induced copper oxide active sites are essential for the preparation of CuO-Cu₂O-ZnO heterojunction structures without the need for catalysts and seed layer coatings.

3.2. Modulating the Morphology of ZnO Nanowires

Figure 4 shows the SEM images of ZnO nanowire morphology obtained under hydrothermal conditions with reactant concentrations of 1 mM, 25 mM, 50 mM, 100 mM, 200 mM, 400 mM, 600 mM, and 800 mM, respectively. From Figure 4a,e, it can be seen that at an initial concentration of 1 mM, the grown ZnO nanowires are extremely short, with a length of about 0.33 μm and a diameter of about 0.13 μm, due to the low concentration of Zn²⁺. When the concentration of reactants exceeds 50 mM, as shown in Figure 4c,g, the length of the ZnO nanowires is 3.55 μm and the diameter is 0.34 μm, and the growing density of ZnO can be seen to have increased tremendously by this time. As shown in Figure 4i,m, when the concentration increases to 200 mM, the length of the ZnO nanowires continues to increase to approximately 4.6 μm and the growth density of the ZnO nanowires is almost maximized, but the nanowires are not uniform, and the coarse and fine ones are mixed, with diameters varying from approximately 0.36 μm to 0.7 μm. As shown in Figure 4j,n, when the growth concentration reaches 400 mM, the morphology of the ZnO nanowires starts to change from a cylindrical rod to a hexagonal prism with a length of 4.7 μm and a diameter of 1.2 μm. There is a small bump on top of the hexagonal prism. As shown in Figure 4k,o, when the concentration exceeds 600 mM, the small bumps on the hexagonal prism disappear, and the morphology of the ZnO nanowires becomes completely hexagonal prismatic and does not change with the increase in concentration.

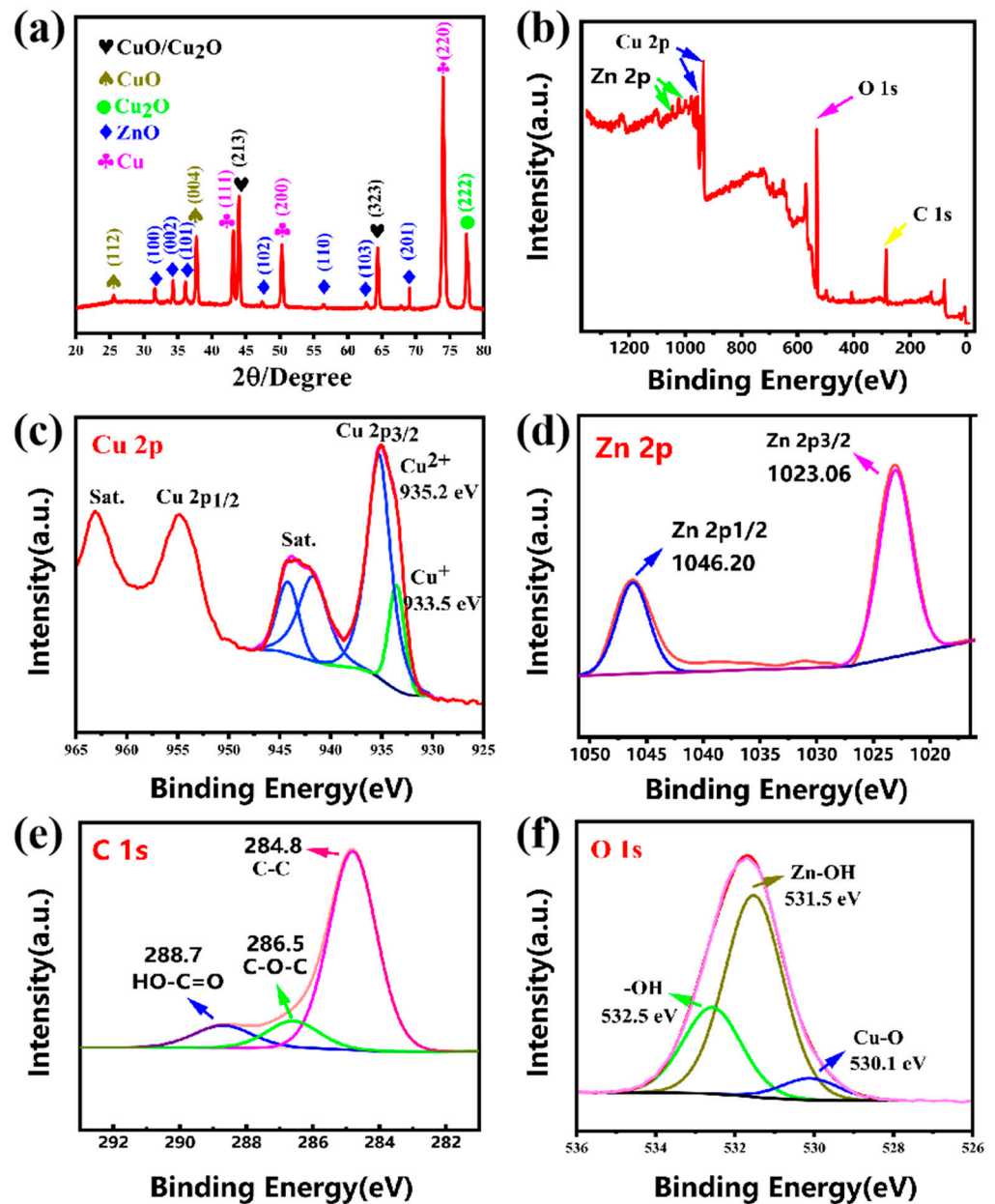


Figure 3. (a) XRD pattern of CuO-Cu₂O-ZnO heterojunction constructed on the copper sheet (sample 3); (b-f) XPS spectra of sample S3; (b) survey; (c) spectrum of Cu 2p; (d) spectrum of Zn 2p; (e) spectrum of C 1s; and (f) spectrum of O 1s.

As shown in Figure 4, it is clear that the orderliness and growth position of ZnO nanorods grown on “grid-type” copper substrates were retained at constant in the eight sets of experiments, but the growing concentration of ZnO caused a dramatic change in the morphology of ZnO nanowires [60]. This effect of reactant concentration on morphology can be understood in terms of the critical concentration difference between the (0001) and (0010) facets of the ZnO nanowires, which is related to the surface energy difference between the crystalline facets. In ZnO nanowires, (0001) polar planes have the highest surface energy (2.0 J/m²) [56] compared to other crystalline planes (e.g., (0010) planes, 1.16 J/m²) [60], and crystalline planes with larger surface energies have lower nucleation-free energy barriers (i.e., lower critical nucleation concentrations). Furthermore, crystal growth occurs when the concentration of reactants exceeds the critical concentration of each

crystalline surface. In the early stages of the hydrothermal reaction, the reactant solution is supersaturated for both the (0001) and (0010) planes, so that ZnO crystals cannot only grow axially but also laterally; however, even in the same concentration of the reaction solution, the ZnO nuclei of the (0001) compared to the (0010) planes also face greater supersaturation, which leads to faster axial growth of ZnO crystals than lateral growth, resulting in the formation of ZnO nanowires with a length greater than the diameter. Furthermore, as the concentration of reactants increases, the supersaturation between the different crystalline planes is lifted relatively more slowly, leading to a continuous increase in the length and diameter of the ZnO nanowires and finally to the formation of ZnO nanowires with different aspect ratios [56,60]. The trends of length, diameter, and aspect ratio of ZnO nanowires grown at growth concentrations from 1 mM to 800 mM are shown in Figure 4q–s. As the growth concentration was increased, the length of the ZnO nanowire increased from 0.33 μm to 5.4 μm and the diameter increased from 0.14 μm to 1.6 μm , with the ZnO nanowire length increasing much faster than the diameter; this growth process of ZnO nanowires can be divided into two stages. In the first growth stage, as the concentration of the reactant increased from 1 mM to 50 mM, the length of the ZnO nanowires increased from 0.33 μm to 3.55 μm ; the most significant change in the length of the ZnO nanowires was observed during this process. In contrast, the diameter of the ZnO nanowires increased more slowly as the concentration increased from 1 mM to 50 mM, and an increase in diameter of the ZnO nanowires was seen from 0.14 μm to 0.34 μm , with the aspect ratio of the ZnO nanowires at 1 mM being 2.35 and increasing with increasing reactant concentration, reaching a maximum aspect ratio of 10.44 at 50 mM. In the second growth stage, as the concentration of reactants increased from 100 mM to 800 mM, the growth rate of the length of the ZnO nanorods began to slow down, increasing from approximately 3.6 μm to 5.4 μm in length. Conversely, the growth rate of the diameter of the ZnO nanorods increased from 0.5 μm to 1.6 μm when the growth concentration was increased from 100 mM to 800 mM. Particularly, when the concentration of reactants increased from 200 mM to over 400 mM, the morphology of ZnO changed from nanowires to hexagonal prisms, and the diameter of the ZnO nanomaterials increased from 0.7 μm to 1.2 μm , so that at these concentrations the most significant change was observed in the diameter of ZnO. Furthermore, the aspect ratio of the ZnO nanorods was 7.22 at a reactant concentration of 100 mM and decreased to 2.62 when the reactant concentration was increased to 800 mM. This demonstrates that different concentrations of reactants cause different growth rates of ZnO nanowires along the radial and axial directions, which ultimately leads to the formation of ZnO nanowires with tunable aspect ratios.

3.3. Piezocatalytic Performance Evaluation

The piezocatalytic activity of the as-prepared samples was analyzed via MB decomposition with ultrasonication in the dark with an initial concentration of MB at 0.6 mg/L [33]. Figure 5a,b shows the piezoelectric catalytic degradation performance of the mixed ZnO nanowire arrays from sample 1 to sample 8. As expected, within a certain range, increasing the growth concentration of ZnO nanowires is beneficial for improving the piezoelectric catalytic degradation of immobilized hybrid ZnO nanowires. Sample 1 was grown at a concentration of 1 mM and had the lowest piezoelectric catalytic degradation performance (8%), while sample 8 was grown at a concentration of 800 mM and had the highest degradation performance (34%). As shown in Figure 4, as the growth concentration was increased, the length of the ZnO nanowire increased from 0.33 μm to 5.4 μm and the diameter increased from 0.14 μm to 1.6 μm ; the increase in length of the ZnO nanowires was much faster than the increase in diameter. The higher piezocatalytic degradation performance of the mixed ZnO nanowire arrays with higher growth concentrations can be attributed to the larger active surface area under external forces from the longer length of the ZnO nanowires; there were more reaction sites for pollutant decomposition. Furthermore, the more significant the increase in the length of the ZnO nanowires, the more likely the ZnO nanowires are to

bend and deform under the same external pressure, determining a more efficient internal migration of electrons and holes, thus leading to better piezoelectric catalytic degradation performance of the ZnO nanowires [18,52].

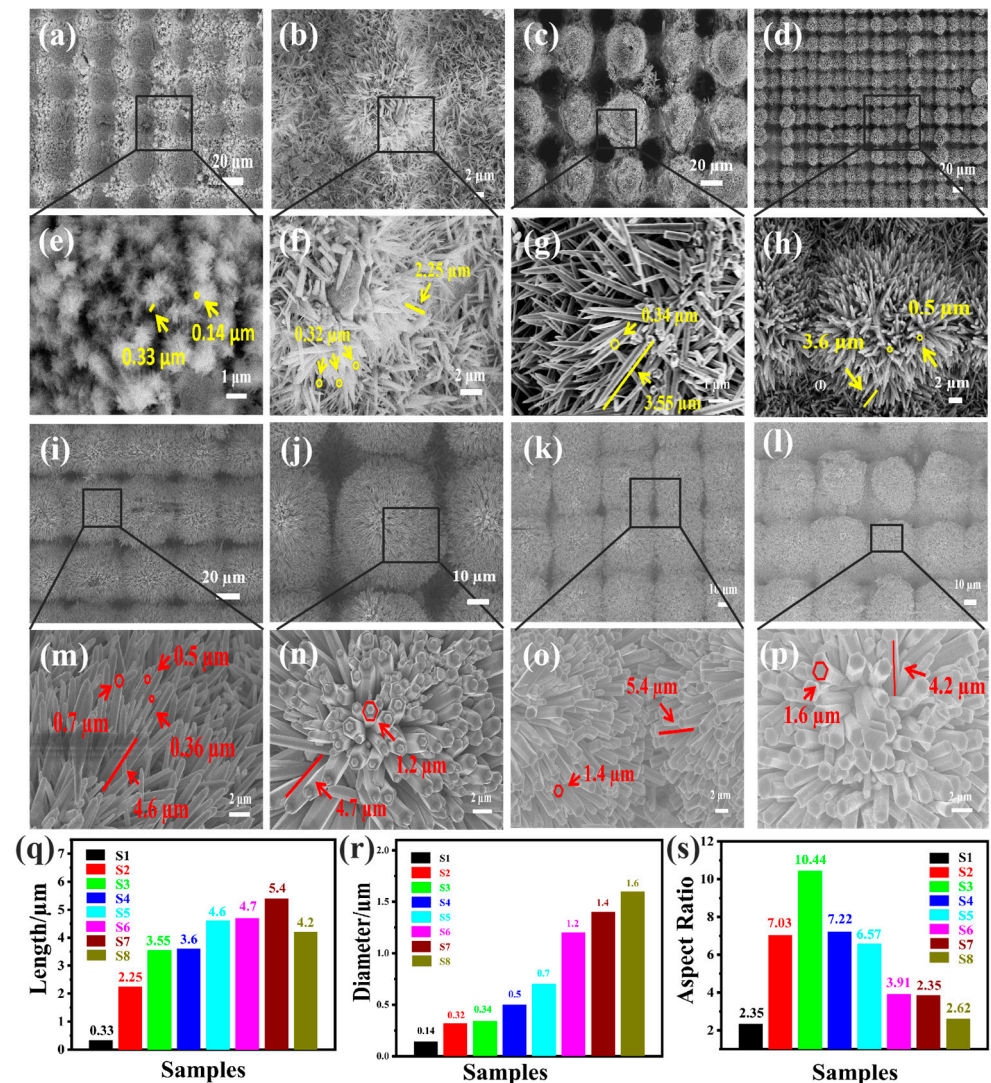


Figure 4. (a–p) SEM images of ZnO grown on “grid-type” substrate using eight different reactant concentrations: (a,e) 1 mM; (b,f) 25 mM; (c,g) 50 mM; (d,h) 100 mM; (i,m) 200 mM; (j,n) 400 mM; (k,o) 600 mM; and (l,p) 800 mM. Growth time: 2 h; growth temperature: 150 °C; (q–s) length, diameter, and aspect ratio statistics of ZnO nanorods grown on “grid-type” substrates for eight reactant concentrations; (q) length; (r) diameter; (s) aspect ratio.

To further evaluate the piezoelectric degradation performance of CuO-Cu₂O-ZnO piezoelectric catalysts, we recorded the UV-Vis absorption spectra of sample 8 during catalytic degradation. The illustration in the top left corner of Figure 5b shows the UV-Vis absorption spectra (500–730 nm) of the MB solution, acquired at different ultrasonic stirring times. It can be observed that the intensity of the maximum absorption peak, located at 664 nm, progressively decreases with the prolongation of the ultrasonic stirring time. Furthermore, in the box of Figure 5b, the MB solutions at increasing ultrasonic stirring times are shown in the top left corner, highlighting how the initial blue color of the MB solution gradually fades, thus fully demonstrating the piezoelectric catalytic capacity of ZnO nanowires grown on copper substrates.

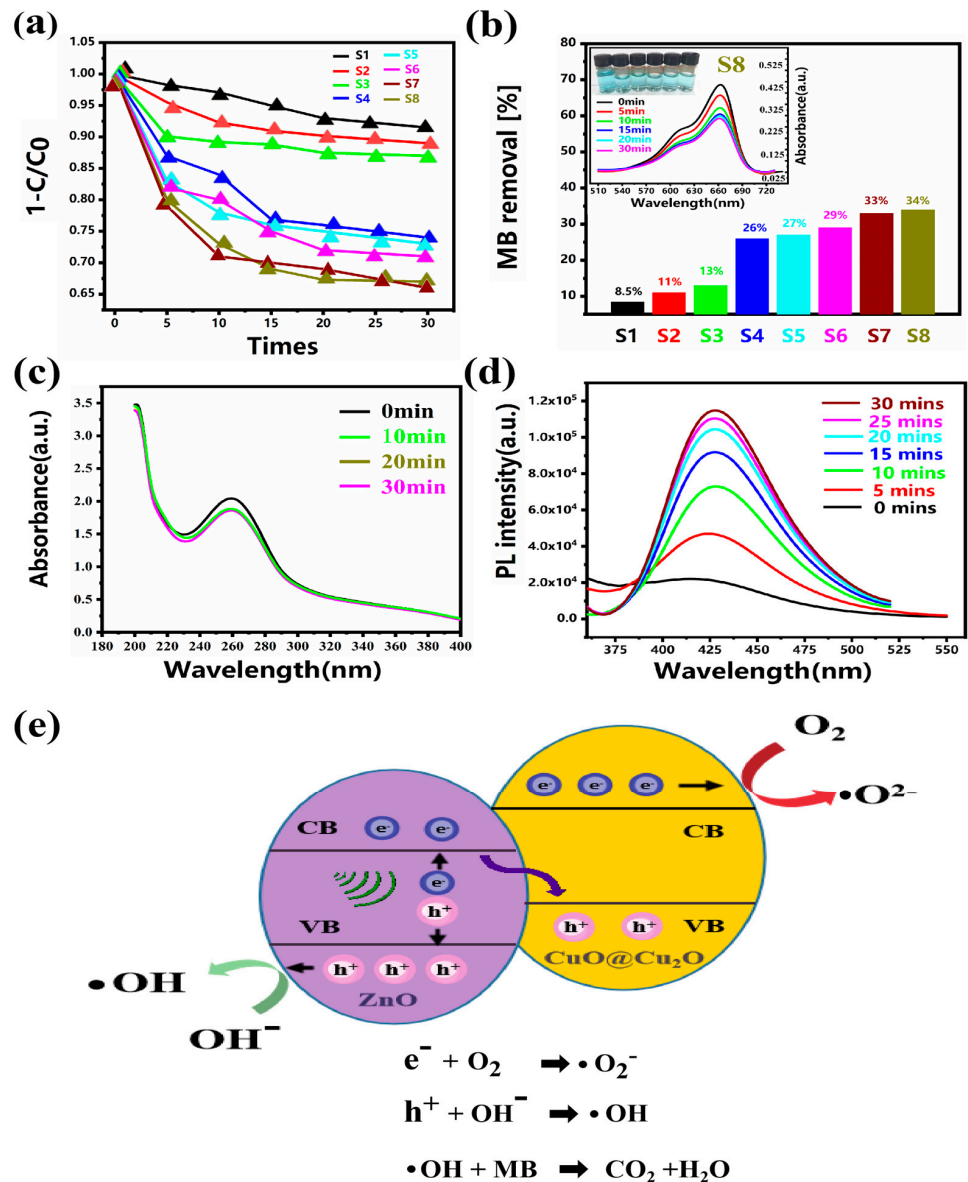


Figure 5. (a) The piezoelectric catalytic degradation process of a group of eight hybrid ZnO samples; (b) statistics of piezoelectric catalytic degradation of a group of eight hybrid ZnO samples for 30 mins. The upper left picture shows the color change in MB solution and UV-Vis absorption spectra of MB dye at different degradation times in the presence of sample S8; (c) fluorescence spectra of TAOH for detecting $\cdot OH$ generated by sample S8 and heterogeneous CuO-Cu₂O-ZnO piezoelectric-catalytic degradation of MB; (d) UV-Vis absorption spectra of NBT for detecting $\cdot O_2^-$ generated by sample S8 and heterogeneous CuO-Cu₂O-ZnO piezoelectric-catalytic degradation of MB; and (e) mechanism of production of reactive oxygen species by CuO-Cu₂O-ZnO heterojunction under the action of ultrasonic waves.

To elucidate the mechanism of piezocatalysis, sample S8 was examined for reactive oxygen species (ROS) produced during piezoelectric catalytic degradation. Hydroxyl radicals and superoxide anions generated during piezoelectric catalysis were detected via the terephthalic acid photoluminescence (TA-PL) method and NBT transformation method, respectively. NBT can react with $\cdot O_2^-$ to form insoluble purple formazan in aqueous solution; therefore, the generated superoxide ions can be determined spectrophotometrically using NBT as a probe by monitoring the concentration changes in NBT because of the catalytic reaction. Figure 5c shows the NBT spectra recorded at different times during

the piezoelectric catalysis process, from 0 min to 30 mins, highlighting the decreasing intensity of the absorbance signal of NBT at 259 nm in the solution. This indicates that the $\cdot\text{O}_2^-$ produced in the piezoelectric catalysis process is involved in the degradation of MB [61,62]. The rapid and selective reaction of terephthalic acid (TA) with $\cdot\text{OH}$ produces highly fluorescent 2-hydroxy terephthalic acid (TAOH), which fluoresces at 429 nm. The PL intensities of TAOH (see Figure 5d), significantly enhanced with the prolonged catalytic reaction time, demonstrate that $\cdot\text{OH}$ radicals are continuously generated in the piezocatalytic process [63,64]. The findings confirm that CuO-Cu₂O-ZnO can efficiently produce $\cdot\text{O}_2^-$ and $\cdot\text{OH}$ for the degradation of pollutants.

The initial occurrence required for the degradation process is the generation of conduction band electrons (e^-) and valence band holes (h^+) (electron-hole pairs) in semiconductors [49]. The mechanism of $\cdot\text{O}_2^-$ and $\cdot\text{OH}$ -activated oxide generation by the CuO-Cu₂O-ZnO hybrid catalyst for the degradation of organic pollutants is shown in Figure 5e. It can be concluded that the efficient piezoelectric catalytic performance of ZnO nanowires on copper sheets can be attributed to the coupling effect of the efficient charge transfer process of the hybrid CuO-Cu₂O-ZnO heterojunction and the piezoelectric field generated by the ZnO nanowires under the action of an ultrasound. Under intense ultrasonic irradiation, the water produces extremely active bubbles, which subsequently collapse and generate localized high water pressure, causing the ZnO nanowires to bend and allowing the ZnO nanowires to generate built-in potential to induce the separation of electrons and holes. As shown in Figure 3c, CuO and Cu₂O are generated after laser processing, and CuO and Cu₂O are p-type semiconductors, while ZnO is an n-type semiconductor. As shown in Figure 5e, when p-type and n-type semiconductors are in contact, the electrons moved from the CB (conduction band) of ZnO to the VB (valence band) of CuO and Cu₂O via electrostatic attraction, which results in the electrons staying in the CB of CuO and Cu₂O and the hole remaining in the VB of ZnO, respectively. This process could reduce the recombination of electron and hole pairs on the surface of ZnO [65]. It has been shown that the CB potential of CuO is -0.92 eV versus the NHE (normal hydrogen electrode) potential, and the CB potential of Cu₂O is -1.2 eV versus the NHE [66], which is more negative than the standard redox potential of $\text{O}_2/\cdot\text{O}_2^-$ (-0.33 eV versus NHE); so, the electrons in the CB of CuO and Cu₂O can reduce the oxygen dissolved in water to produce $\cdot\text{O}_2^-$. Meanwhile, the VB potential of ZnO ($+3.01$ eV versus NHE) is more positive than the standard redox potential of $\cdot\text{OH}/\text{H}_2\text{O}$ ($+2.38$ eV versus NHE), and so the holes in the VB of ZnO can oxidize H_2O to produce $\cdot\text{OH}$. Under the coupling effect of the efficient charge transfer process of the hybrid ZnO heterojunction and the piezoelectric field generated via the bending of ZnO nanorods, a large number of reactive oxygen species (ROS) are generated in the hybrid catalytic degradation system, in which hydroxyl radicals can oxidize methylene blue in water to produce non-toxic CO_2 and H_2O . Figure 5e [67] shows the reaction equations associated with the process.

4. Conclusions

In this work, immobilized CuO-Cu₂O-ZnO hybrid catalysts were fabricated on a 3D CuO-Cu₂O-Cu substrate via the laser-processing-technology-assisted hydrothermal method without any catalyst or seed layer coating before the hydrothermal reaction. A periodic three-dimensional CuO-Cu₂O-Cu substrate was firstly fabricated via laser ablation, followed by the hydrothermal-synthesis-induced growth of ZnO nanowires on a 3D CuO-Cu₂O-Cu substrate for the formation of a CuO-Cu₂O-ZnO heterojunction structure. The laser processing parameters were optimized for favorable ZnO growth. The surface morphology and chemical composition of CuO-Cu₂O-ZnO hybrid catalysts were characterized using SEM, XRD, and XPS techniques, indicating the successful preparation of CuO-Cu₂O-ZnO heterojunction catalysts on a grid-type substrate. Furthermore, it was found that the formation of Cu₂O-CuO on the copper sheet via laser processing was crucial for the preparation of the CuO-Cu₂O-ZnO heterojunction catalyst. The process of change in the morphology of ZnO nanowires and their physical mechanisms were investigated

in detail using reactant concentrations ranging from 1 mM to 800 mM. ZnO nanorods on “grid-type” copper substrates demonstrated effective piezoelectric catalytic abilities with different morphologies, and it was found that longer ZnO nanowires have a stronger piezoelectric catalytic degradation performance. This can be attributed to the fact that the longer the length of the ZnO nanowires, the greater the active surface area under external forces, providing more reaction sites for pollutant decomposition. Furthermore, the easier it is to bend and deform the ZnO nanowire under the same external pressure, the more efficient the internal migration of electrons and holes is, which leads to better piezoelectric catalytic degradation performance of ZnO nanowires. Abundant reactive oxygen species were detected in the hybrid piezoelectric ZnO catalysis system, which indicates that the catalytic piezoelectric pathway degrades organic compounds in water. This simple and low-cost method could provide a useful guide for the large-scale efficient and versatile synthesis of immobilized piezoelectric catalysts for the water redemption industry.

Author Contributions: Conceptualization, R.Z.; Data Curation, H.W.; Funding Acquisition, R.Z.; Investigation, H.W.; Resources, H.Y.; Supervision, H.L.; Writing—Original Draft, H.W.; Writing—Review and Editing, R.Z. and H.L. All authors have read and agreed to the published version of the manuscript.

Funding: This work was supported by the National Natural Science Foundation of China (no. 62175203), the Fujian Provincial Science and Technology Program (no. 2020H0006), and the Innovation Laboratory for Sciences and Technologies of Energy Materials of Fujian Province Applied Research Project (no. RD2020050301).

Institutional Review Board Statement: Not applicable.

Informed Consent Statement: Not applicable.

Data Availability Statement: The data are available from the corresponding author on reasonable request.

Conflicts of Interest: The authors declare that they have no known competing financial interests or personal relationships that could have appeared to influence the work reported in this paper.

References

1. Ma, J.; Ren, J.; Jia, Y.; Wu, Z.; Chen, L.; Haugen, N.O.; Huang, H.; Liu, Y. High efficiency bi-harvesting light/vibration energy using piezoelectric zinc oxide nanorods for dye decomposition. *Nano Energy* **2019**, *62*, 376–383. [[CrossRef](#)]
2. Xiang, D.; Liu, Z.; Wu, M.; Liu, H.; Zhang, X.; Wang, Z.; Wang Zhong, L.; Li, L. Enhanced Piezo-Photoelectric Catalysis with Oriented Carrier Migration in Asymmetric Au-ZnO Nanorod Array. *Small* **2020**, *16*, 1907603. [[CrossRef](#)]
3. Gao, Y.; Li, S.; Zhao, B.; Thai, Q.; Lita, A.; Dalal, N.S.; Kroto, H.W.; Acquah, S.F.A. A synergistic approach to light-free catalysis using zinc oxide embedded multi-walled carbon nanotube paper. *Carbon* **2014**, *77*, 705–709. [[CrossRef](#)]
4. Chen, L.; Jia, Y.; Zhao, J.; Ma, J.; Wu, Z.; Yuan, G.; Cui, X. Strong piezocatalysis in barium titanate/carbon hybrid nanocomposites for dye wastewater decomposition. *J. Colloid Interface Sci.* **2021**, *586*, 758–765. [[CrossRef](#)]
5. Jia, S.; Su, Y.; Zhang, B.; Zhao, Z.; Li, S.; Zhang, Y.; Li, P.; Xu, M.; Ren, R. Few-layer MoS₂ nanosheet-coated KNbO₃ nanowire heterostructures: Piezo-photocatalytic effect enhanced hydrogen production and organic pollutant degradation. *Nanoscale* **2019**, *11*, 7690–7700. [[CrossRef](#)] [[PubMed](#)]
6. Wu, H.; Jile, H.; Chen, Z.; Xu, D.; Yi, Z.; Chen, X.; Chen, J.; Yao, W.; Wu, P.; Yi, Y. Fabrication of ZnO@MoS₂ Nanocomposite Heterojunction Arrays and Their Photoelectric Properties. *Micromachines* **2020**, *11*, 189. [[CrossRef](#)] [[PubMed](#)]
7. Gao, C.; Sun, Z.; Li, K.; Chen, Y.; Cao, Y.; Zhang, S.; Feng, L. Integrated oil separation and water purification by a double-layer TiO₂-based mesh. *Energy Environ. Sci.* **2013**, *6*, 1147–1151. [[CrossRef](#)]
8. Zhang, S.; Liu, Z.; Ruan, M.; Guo, Z.; E, L.; Zhao, W.; Zhao, D.; Wu, X.; Chen, D. Enhanced piezoelectric-effect-assisted photoelectrochemical performance in ZnO modified with dual cocatalysts. *Appl. Catal. B-Environ.* **2020**, *262*, 118279. [[CrossRef](#)]
9. Xie, Y.; Wang, S.; Lin, L.; Jing, Q.; Lin, Z.-H.; Niu, S.; Wu, Z.; Wang, Z.L. Rotary Triboelectric Nanogenerator Based on a Hybridized Mechanism for Harvesting Wind Energy. *Acs Nano* **2013**, *7*, 7119–7125. [[CrossRef](#)] [[PubMed](#)]
10. Bai, S.; Zhang, L.; Xu, Q.; Zheng, Y.; Qin, Y.; Wang, Z.L. Two dimensional woven nanogenerator. *Nano Energy* **2013**, *2*, 749–753. [[CrossRef](#)]
11. Wang, X.; Song, J.; Liu, J.; Wang, Z.L. Direct-current nanogenerator driven by ultrasonic waves. *Science* **2007**, *316*, 102–105. [[CrossRef](#)]
12. Wang, L.; Liu, S.; Wang, Z.; Zhou, Y.; Qin, Y.; Wang, Z.L. Piezotronic Effect Enhanced Photocatalysis in Strained Anisotropic ZnO/TiO₂ Nanoplatelets via Thermal Stress. *Acs Nano* **2016**, *10*, 2636–2643. [[CrossRef](#)] [[PubMed](#)]

13. Yang, Y.; Pradel, K.C.; Jing, Q.; Wu, J.M.; Zhang, F.; Zhou, Y.; Zhang, Y.; Wang, Z.L. Thermoelectric Nanogenerators Based on Single Sb-Doped ZnO Micro/Nanobelts. *Acs Nano* **2012**, *6*, 6984–6989. [[CrossRef](#)] [[PubMed](#)]
14. Yin, B.; Qiu, Y.; Zhang, H.; Ji, J.; Lei, J.; Luo, Y.; Zhao, Y.; Hu, L. Piezoelectric nanogenerator with 3D-ZnO micro-thornyballs prepared by chemical vapour deposition. *J. Mater. Sci. -Mater. Electron.* **2015**, *26*, 742–746. [[CrossRef](#)]
15. Xu, S.; Wei, Y.; Liu, J.; Yang, R.; Wang, Z.L. Integrated Multilayer Nanogenerator Fabricated Using Paired Nanotip-to-Nanowire Brushes. *Nano Lett.* **2008**, *8*, 4027–4032. [[CrossRef](#)]
16. Zhang, F.; Ding, Y.; Zhang, Y.; Zhang, X.; Wang, Z.L. Piezo-phototronic Effect Enhanced Visible and Ultraviolet Photodetection Using a ZnO-CdS Core-Shell Micro/nanowire. *Acs Nano* **2012**, *6*, 9229–9236. [[CrossRef](#)]
17. Xiong, D.; Deng, W.; Tian, G.; Gao, Y.; Chu, X.; Yan, C.; Jin, L.; Su, Y.; Yan, W.; Yang, W. A piezo-phototronic enhanced serrate-structured ZnO-based heterojunction photodetector for optical communication. *Nanoscale* **2019**, *11*, 3021–3027. [[CrossRef](#)]
18. Hong, K.-S.; Xu, H.; Konishi, H.; Li, X. Direct Water Splitting Through Vibrating Piezoelectric Microfibers in Water. *J. Phys. Chem. Lett.* **2010**, *1*, 997–1002. [[CrossRef](#)]
19. Wang, P.; Tang, Q.; Zhang, L.; Xu, M.; Sun, L.; Sun, S.; Zhang, J.; Wang, S.; Liang, X. Ultrasmall Barium Titanate Nanoparticles for Highly Efficient Hypoxic Tumor Therapy via Ultrasound Triggered Piezocatalysis and Water Splitting. *Acs Nano* **2021**, *15*, 11326–11340. [[CrossRef](#)] [[PubMed](#)]
20. Xu, X.; Jia, Y.; Xiao, L.; Wu, Z. Strong vibration-catalysis of ZnO nanorods for dye wastewater decolorization via piezo-electro-chemical coupling. *Chemosphere* **2018**, *193*, 1143–1148. [[CrossRef](#)]
21. Hong, D.; Zang, W.; Guo, X.; Fu, Y.; He, H.; Sun, J.; Xing, L.; Liu, B.; Xue, X. High Piezo-photocatalytic Efficiency of CuS/ZnO Nanowires Using Both Solar and Mechanical Energy for Degrading Organic Dye. *ACS Appl. Mater. Interfaces* **2016**, *8*, 21302–21314. [[CrossRef](#)] [[PubMed](#)]
22. Li, S.; Zhang, M.; Gao, Y.; Bao, B.; Wang, S. ZnO-Zn/CNT hybrid film as light-free nanocatalyst for degradation reaction. *Nano Energy* **2013**, *2*, 1329–1336. [[CrossRef](#)]
23. Li, B.; Wang, Y. Facile Synthesis and Enhanced Photocatalytic Performance of Flower-like ZnO Hierarchical Microstructures. *J. Phys. Chem. C* **2010**, *114*, 890–896. [[CrossRef](#)]
24. Alenezi, M.R.; Henley, S.J.; Emerson, N.G.; Silva, S.R.P. From 1D and 2D ZnO nanostructures to 3D hierarchical structures with enhanced gas sensing properties. *Nanoscale* **2014**, *6*, 235–247. [[CrossRef](#)]
25. Xu, P.; Wang, P.; Wang, Q.; Wei, R.; Li, Y.; Xin, Y.; Zheng, T.; Hu, L.; Wang, X.; Zhang, G. Facile synthesis of Ag₂O/ZnO/rGO heterojunction with enhanced photocatalytic activity under simulated solar light: Kinetics and mechanism. *J. Hazard. Mater.* **2021**, *403*, 124011. [[CrossRef](#)]
26. Huan, H.; Jile, H.; Tang, Y.; Li, X.; Yi, Z.; Gao, X.; Chen, X.; Chen, J.; Wu, P. Fabrication of ZnO@Ag@Ag₃PO₄ Ternary Heterojunction: Superhydrophilic Properties, Antireflection and Photocatalytic Properties. *Micromachines* **2020**, *11*, 309. [[CrossRef](#)]
27. Wang, H.; Zhang, L.; Chen, Z.; Hu, J.; Li, S.; Wang, Z.; Liu, J.; Wang, X. Semiconductor heterojunction photocatalysts: Design, construction, and photocatalytic performances. *Chem. Soc. Rev.* **2014**, *43*, 5234–5244. [[CrossRef](#)] [[PubMed](#)]
28. Yuan, J.; Huang, X.; Zhang, L.; Gao, F.; Lei, R.; Jiang, C.; Feng, W.; Liu, P. Tuning piezoelectric field for optimizing the coupling effect of piezo-photocatalysis. *Appl. Catal. B-Environ.* **2020**, *278*, 119291. [[CrossRef](#)]
29. Guo, X.; Fu, Y.; Hong, D.; Yu, B.; He, H.; Wang, Q.; Xing, L.; Xue, X. High-efficiency sono-solar-induced degradation of organic dye by the piezophototronic/photocatalytic coupling effect of FeS/ZnO nanoarrays. *Nanotechnology* **2016**, *27*, 375704. [[CrossRef](#)] [[PubMed](#)]
30. Sahay, R.; Sundaramurthy, J.; Kumar, P.S.; Thavasi, V.; Mhaisalkar, S.G.; Ramakrishna, S. Synthesis and characterization of CuO nanofibers, and investigation for its suitability as blocking layer in ZnO NPs based dye sensitized solar cell and as photocatalyst in organic dye degradation. *J. Solid State Chem.* **2012**, *186*, 261–267. [[CrossRef](#)]
31. Li, P.; Zhou, Y.; Zhao, Z.; Xu, Q.; Wang, X.; Xiao, M.; Zou, Z. Hexahedron Prism-Anchored Octahedron CeO₂: Crystal Facet-Based Homo Junction Promoting Efficient Solar Fuel Synthesis. *J. Am. Chem. Soc.* **2015**, *137*, 9547–9550. [[CrossRef](#)]
32. Zhang, Y.; Wang, S.; Zhao, Y.; Ding, Y.; Zhang, Z.; Jiang, T.; Wang, Z.L.; Li, L. Piezo-phototronic effect boosted catalysis in plasmonic bimetallic ZnO heterostructure with guided fermi level alignment. *Mater. Today Nano* **2022**, *18*, 375704. [[CrossRef](#)]
33. Ma, W.; Lv, M.; Cao, F.; Fang, Z.; Feng, Y.; Zhang, G.; Yang, Y.; Liu, H. Synthesis and characterization of ZnO-GO composites with their piezoelectric catalytic and antibacterial properties. *J. Environ. Chem. Eng.* **2022**, *10*, 107840. [[CrossRef](#)]
34. Fageria, P.; Gangopadhyay, S.; Pande, S. Synthesis of ZnO/Au and ZnO/Ag nanoparticles and their photocatalytic application using UV and visible light. *RSC Adv.* **2014**, *4*, 24962–24972. [[CrossRef](#)]
35. Guo, M.; Diao, P.; Cai, S.M. Hydrothermal growth of well-aligned ZnO nanorod arrays: Dependence of morphology and alignment ordering upon preparing conditions. *J. Solid State Chem.* **2005**, *178*, 1864–1873. [[CrossRef](#)]
36. Pauporte, T.; Lincot, D. Heteroepitaxial electrodeposition of zinc oxide films on gallium nitride. *Appl. Phys. Lett.* **1999**, *75*, 3817–3819. [[CrossRef](#)]
37. Scarpellini, D.; Paoloni, S.; Medaglia, P.G.; Pizzoferrato, R.; Orsini, A.; Falconi, C. Structural and optical properties of dense vertically aligned ZnO Mark nanorods grown onto silver and gold thin films by galvanic effect with iron contamination. *Mater. Res. Bull.* **2015**, *65*, 231–237. [[CrossRef](#)]
38. Zheng, Z.; Lim, Z.S.; Peng, Y.; You, L.; Chen, L.; Wang, J. General Route to ZnO Nanorod Arrays on Conducting Substrates via Galvanic-cell-based approach. *Sci. Rep.* **2013**, *3*, 2434. [[CrossRef](#)] [[PubMed](#)]

39. Yong, J.; Yang, Q.; Guo, C.; Chen, F.; Hou, X. A review of femtosecond laser-structured superhydrophobic or underwater superoleophobic porous surfaces/materials for efficient oil/water separation. *RSC Adv.* **2019**, *9*, 12470–12495. [[CrossRef](#)]
40. Guo, Y.; Zhang, C.; Chen, Y.; Nie, Z. Research Progress on the Preparation and Applications of Laser-Induced Graphene Technology. *Nanomaterials* **2022**, *12*, 2336. [[CrossRef](#)]
41. Tour, J. Laser-induced graphene. *Abstr. Pap. Am. Chem. Soc.* **2019**, *257*, 1609–1620.
42. Wu, M.L.; Ren, C.Z.; Xu, H.Z.; Zhou, C.L. Fabrication of a bionic microstructure on a C/SiC brake lining surface: Positive applications of surface defects for surface wetting control. *Appl. Surf. Sci.* **2018**, *440*, 669–679. [[CrossRef](#)]
43. Kisala, J.; Gnilitzkyi, I.; Cieniek, B.; Krzeminski, P.; Marchewka, M.; Barylyak, A.; Bobitski, Y. Synthesis of Micro-Spikes and Herringbones Structures by Femtosecond Laser Pulses on a Titanium Plate—A New Material for Water Organic Pollutants Degradation. *Materials* **2021**, *14*, 5556. [[CrossRef](#)] [[PubMed](#)]
44. Zhou, R.; Shen, F.; Cui, J.; Zhang, Y.; Yan, H.; Carlos, S.S.J. Electrophoretic Deposition of Graphene Oxide on Laser-Ablated Copper Mesh for Enhanced Oil/Water Separation. *Coatings* **2019**, *9*, 157. [[CrossRef](#)]
45. Zhou, R.; Lin, S.; Shen, F.; Khew, S.Y.; Hong, M. A universal copper mesh with on-demand wettability fabricated by pulsed laser ablation for oil/water separation. *Surf. Coat. Technol.* **2018**, *348*, 73–80. [[CrossRef](#)]
46. Liu, Y.-L.; Wu, J.M. Synergistically catalytic activities of BiFeO₃/TiO₂ core-shell nanocomposites for degradation of organic dye molecule through piezophototronic effect. *Nano Energy* **2019**, *56*, 74–81. [[CrossRef](#)]
47. Kuznetsov, G.V.; Feoktistov, D.V.; Orlova, E.G.; Batishcheva, K.; Ilenok, S.S. Unification of the textures formed on aluminum after laser treatment. *Appl. Surf. Sci.* **2019**, *469*, 974–982. [[CrossRef](#)]
48. Xu, K.; Zhang, C.; Zhou, R.; Ji, R.; Hong, M. Hybrid micro/nano-structure formation by angular laser texturing of Si surface for surface enhanced Raman scattering. *Opt. Express* **2016**, *24*, 10352–10358. [[CrossRef](#)]
49. Tian, J.-H.; Hu, J.; Li, S.-S.; Zhang, F.; Liu, J.; Shi, J.; Li, X.; Tian, Z.-Q.; Chen, Y. Improved seedless hydrothermal synthesis of dense and ultralong ZnO nanowires. *Nanotechnology* **2011**, *22*, 245601. [[CrossRef](#)]
50. Weintraub, B.; Deng, Y.; Wang, Z.L. Position-controlled seedless growth of ZnO nanorod arrays on a polymer substrate via wet chemical synthesis. *J. Phys. Chem. C* **2007**, *111*, 10162–10165. [[CrossRef](#)]
51. Pham Van, T.; Le Thi Quynh, N.; Hong Hanh, M.; Nguyen Viet, T.; Sai Cong, D.; Nguyen Canh, V.; Do Trung, K. Zinc Oxide Nanorods Grown on Printed Circuit Board for Extended-Gate Field-Effect Transistor pH Sensor. *J. Electron. Mater.* **2017**, *46*, 3732–3737. [[CrossRef](#)]
52. Zhang, Y.; Huang, X.; Yeom, J. A Floatable Piezo-Photocatalytic Platform Based on Semi-Embedded ZnO Nanowire Array for High-Performance Water Decontamination. *Nano-Micro Lett.* **2019**, *11*, 11. [[CrossRef](#)] [[PubMed](#)]
53. Han, Y.; Weng, Z.; Cao, L.; Li, L.; Liang, K.; Lian, Z.; Xu, J.; Wang, Y.; Zhang, Y.; Song, Z.; et al. Fabrication of oil-water separation stainless steel mesh via direct laser interference lithography, candle soot deposition, and thermal treatment. *J. Laser Appl.* **2019**, *31*, 012003. [[CrossRef](#)]
54. Khew, S.Y.; Tan, C.F.; Yan, H.; Lin, S.; Thian, E.S.; Zhou, R.; Hong, M. Nanosecond laser ablation for enhanced adhesion of CuO nanowires on copper substrate and its application for oil-water separation. *Appl. Surf. Sci.* **2019**, *465*, 995–1002. [[CrossRef](#)]
55. Yan, H.; Xiao, X.; Chen, Z.; Chen, Y.; Zhou, R.; Wang, Z.; Hong, M. Realization of adhesion enhancement of CuO nanowires growth on copper substrate by laser texturing. *Opt. Laser Technol.* **2019**, *119*, 012003. [[CrossRef](#)]
56. He, Y.; Yanagida, T.; Nagashima, K.; Zhuge, F.; Meng, G.; Xu, B.; Klamchuen, A.; Rahong, S.; Kanai, M.; Li, X.; et al. Crystal-Plane Dependence of Critical Concentration for Nucleation on Hydrothermal ZnO Nanowires. *J. Phys. Chem. C* **2013**, *117*, 1197–1203. [[CrossRef](#)]
57. Singh, J.; Juneja, S.; Soni, R.K.; Bhattacharya, J. Sunlight mediated enhanced photocatalytic activity of TiO₂ nanoparticles functionalized CuO-Cu₂O nanorods for removal of methylene blue and oxytetracycline hydrochloride. *J. Colloid Interface Sci.* **2021**, *590*, 60–71. [[CrossRef](#)]
58. Shu, X.; Zheng, H.; Xu, G.; Zhao, J.; Cui, L.; Cui, J.; Qin, Y.; Wang, Y.; Zhang, Y.; Wu, Y. The anodization synthesis of copper oxide nanosheet arrays and their photoelectrochemical properties. *Appl. Surf. Sci.* **2017**, *412*, 505–516. [[CrossRef](#)]
59. Sun, S.; Zhang, X.; Song, X.; Liang, S.; Wang, L.; Yang, Z. Bottom-up assembly of hierarchical Cu₂O nanospheres: Controllable synthesis, formation mechanism and enhanced photochemical activities. *Crytengcomm* **2012**, *14*, 3545–3553. [[CrossRef](#)]
60. Wang, L.; Wei, Y.; Chen, C.; Yang, S. One-dimensional ZnO micro/nanostructures: Deep insight into the growth mechanism and fine control of the microscopic morphology. *Dalton Trans.* **2021**, *50*, 3011–3019. [[CrossRef](#)] [[PubMed](#)]
61. Ma, W.; Yao, B.; Zhang, W.; He, Y.; Yu, Y.; Niu, J. Fabrication of PVDF-based piezocatalytic active membrane with enhanced oxytetracycline degradation efficiency through embedding few-layer E-MoS₂ nanosheets. *Chem. Eng. J.* **2021**, *415*, 129000. [[CrossRef](#)]
62. Zhao, Y.; Low, Z.-X.; Pan, Y.; Zhong, Z.; Gao, G. Universal water disinfection by piezoelectret aluminium oxide-based electroporation and generation of reactive oxygen species. *Nano Energy* **2022**, *92*, 106749. [[CrossRef](#)]
63. Wan, L.; Tian, W.; Li, N.; Chen, D.; Xu, Q.; Li, H.; He, J.; Lu, J. Hydrophilic porous PVDF membrane embedded with BaTiO₃ featuring controlled oxygen vacancies for piezocatalytic water cleaning. *Nano Energy* **2022**, *94*, 106930. [[CrossRef](#)]
64. Wang, Y.; Xu, Y.; Dong, S.; Wang, P.; Chen, W.; Lu, Z.; Ye, D.; Pan, B.; Wu, D.; Vecitis, C.D.; et al. Ultrasonic activation of inert poly(tetrafluoroethylene) enables piezocatalytic generation of reactive oxygen species. *Nat. Commun.* **2021**, *12*, 3508. [[CrossRef](#)]
65. Ruan, S.; Huang, W.; Zhao, M.; Song, H.; Gao, Z. A Z-scheme mechanism of the novel ZnO/CuO n-n heterojunction for photocatalytic degradation of Acid Orange 7. *Mater. Sci. Semicond. Process.* **2020**, *107*, 104835. [[CrossRef](#)]

66. Siripala, W.; Ivanovskaya, A.; Jaramillo, T.F.; Baeck, S.H.; McFarland, E.W. A $\text{Cu}_2\text{O}/\text{TiO}_2$ heterojunction thin film cathode for photoelectrocatalysis. *Sol. Energy Mater. Sol. Cells* **2003**, *77*, 229–237. [[CrossRef](#)]
67. Xue, X.; Zang, W.; Deng, P.; Wang, Q.; Xing, L.; Zhang, Y.; Wang, Z.L. Piezo-potential enhanced photocatalytic degradation of organic dye using ZnO nanowires. *Nano Energy* **2015**, *13*, 414–422. [[CrossRef](#)]

Disclaimer/Publisher’s Note: The statements, opinions and data contained in all publications are solely those of the individual author(s) and contributor(s) and not of MDPI and/or the editor(s). MDPI and/or the editor(s) disclaim responsibility for any injury to people or property resulting from any ideas, methods, instructions or products referred to in the content.